Supplementary Files

Nano-engineering and functionalization of hybrid Au-Me_xO_y-TiO_2 (Me=W, Ga) hetero-interfaces for optoelectronic receptors and nociceptors

Hongyan Xu, [+a] Mohammad Karbalaei Akbari, [b, c +]* Francis Verpoort, [b,e] and Serge Zhuiykov,[b,c]*

[a]*School of Materials Science & Engineering, North University of China, Taiyuan, 030051 Shanxi, PR China*

[b]*Centre for Environmental & Energy Research, Ghent University, Global Campus, 21985, Incheon, South Korea.*

[c]*Department of Solid State Sciences, Faculty of Science, Ghent University, 9000 Ghent, Belgium.*

[d]*State Key Laboratory of Advanced Technology for Materials Synthesis & Processing, Wuhan University of Technology, Wuhan, 630070, PR China*

[+] Hongyan Xu and Mohammad Karbalaei Akbari contributed equally to this work.

*Corresponding author. E-mail: Serge.Zhuiykov@Ugent.be; Mohammad.akbari@ugent.be

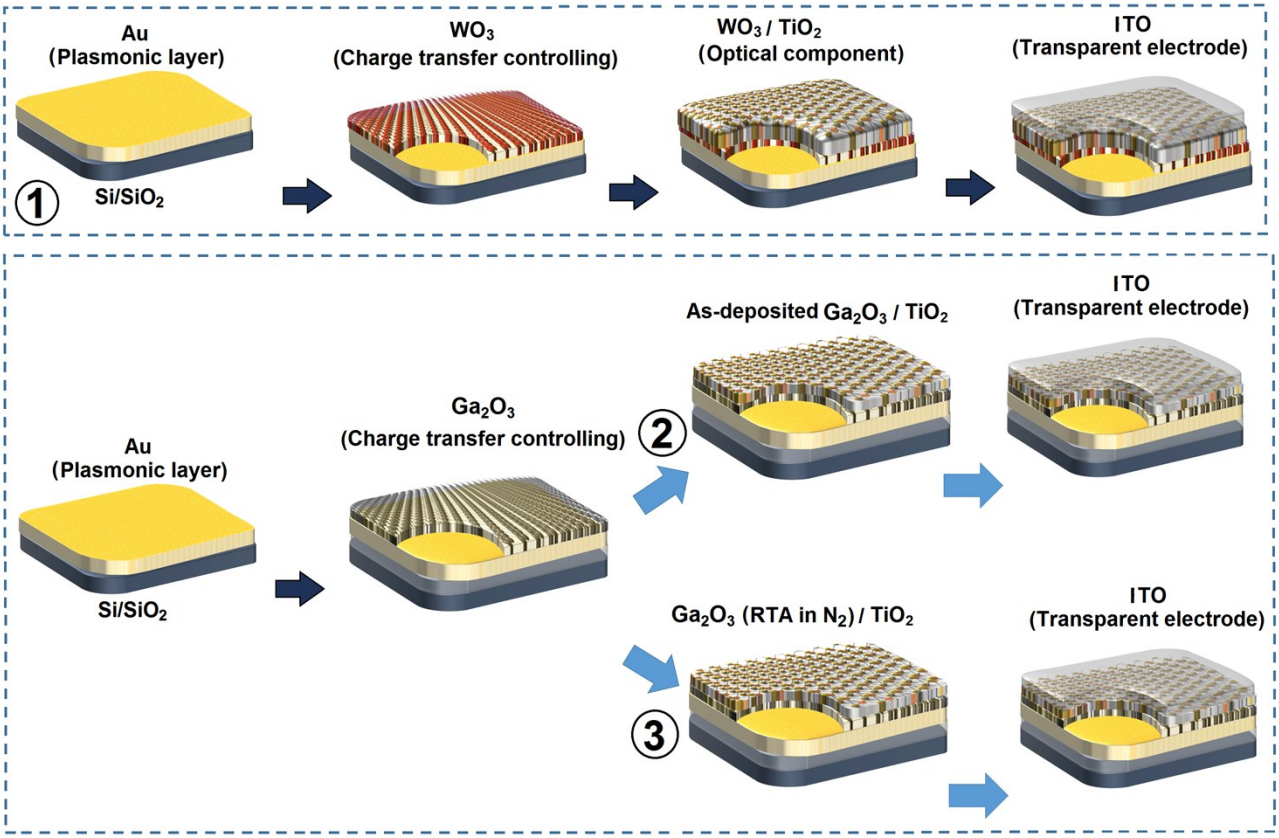

Supplementary Figure S1. Various developed optoelectronic devices based on (1) Au/WO_3:TiO_2/ITO, (2) Au/Ga_2O_3:TiO_2/ITO and (3) Au/Ga_2O_3 (N_2):TiO_2/ITO heterostructures.

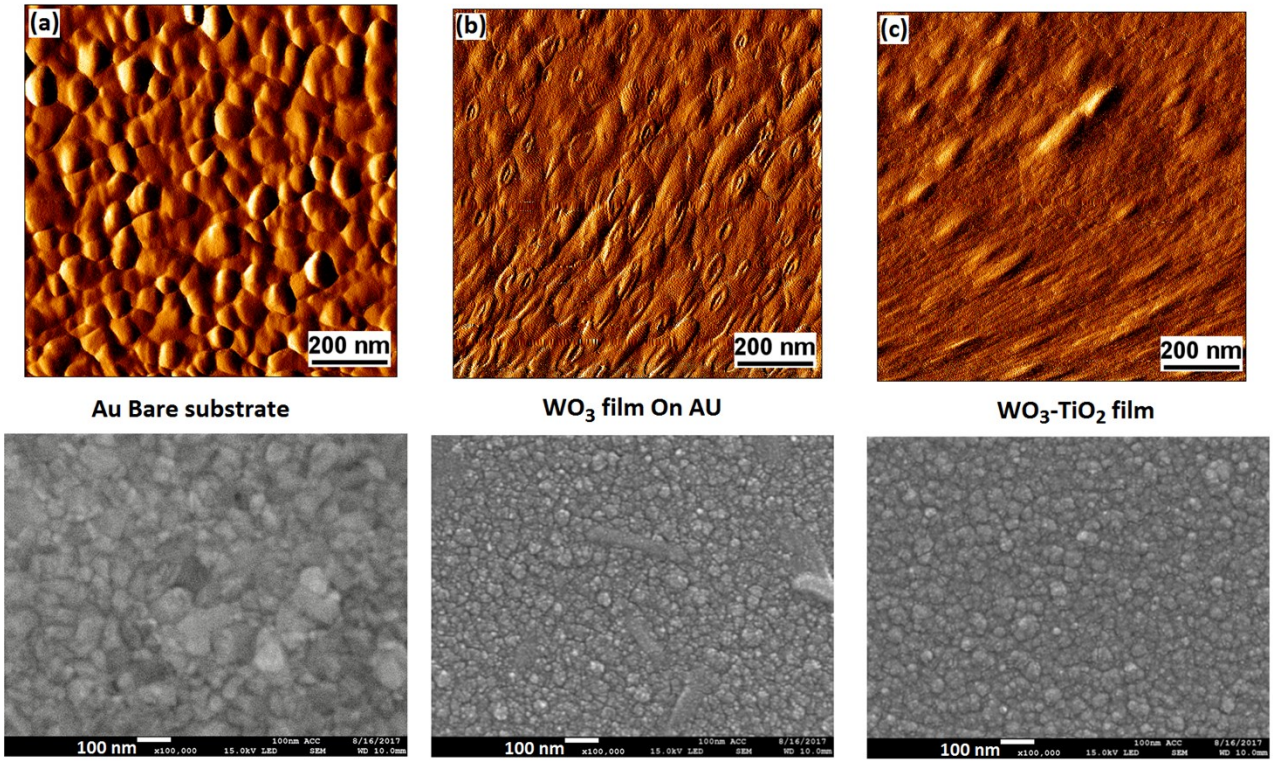

Supplementary Figure S2. Sequential stage of deposition of WO_3:TiO_2 heterostructured film. (a) AFM (top) and FESEM image (down) of surface of bare Au film. The bare surface of Au substrate composed of granular Au structures (b) AFM image (top) and FESEM image (down) of WO_3 film deposited on Au substrate. Ultra-thin WO_3 film covered the surface of granular Au film. (c) AFM image (top) and FESEM image (down) of WO_3:TiO_2 heterostructured film. Both WO_3 and TiO_2 film have ultra-fine granular morphology.

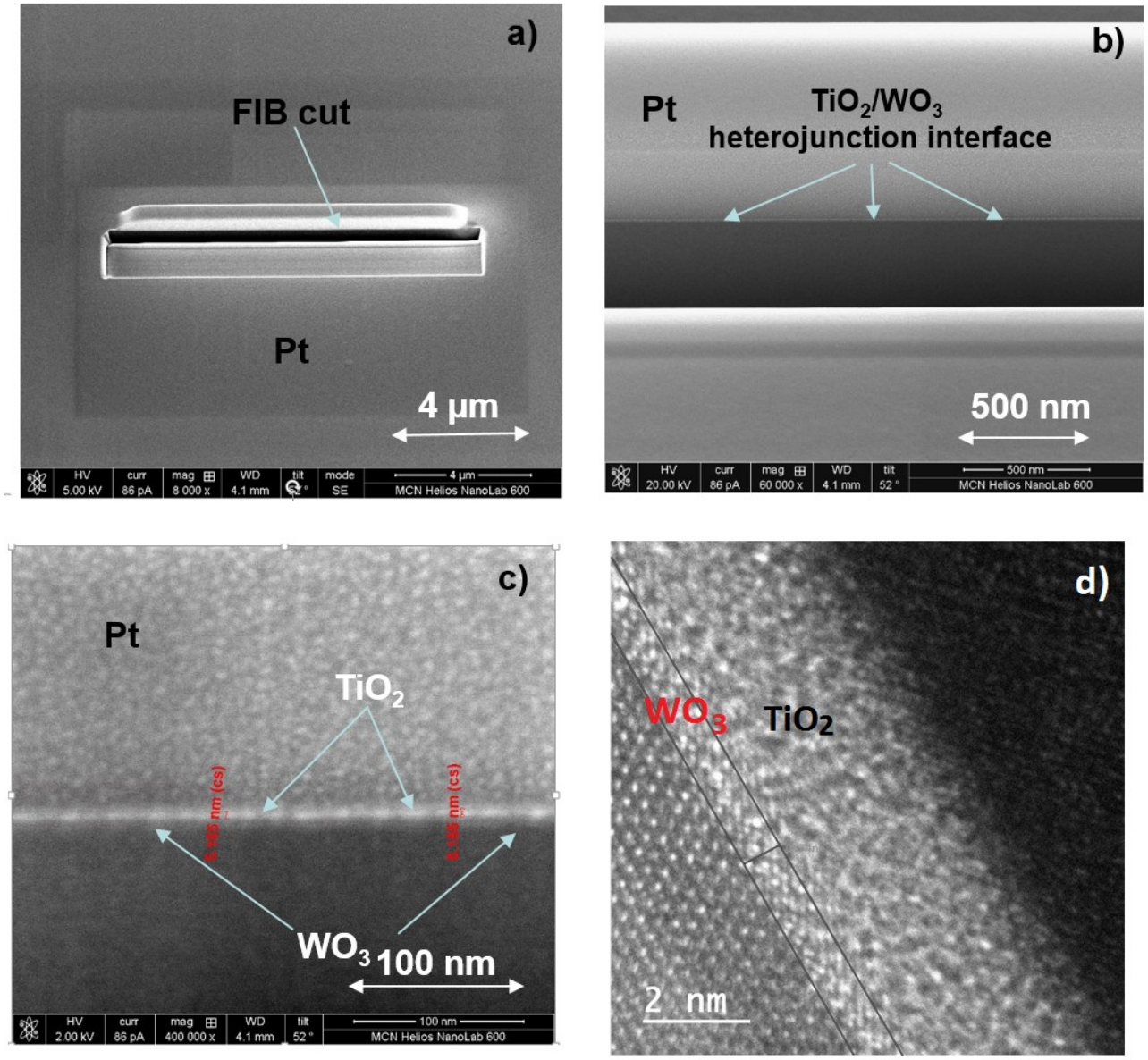

Supplementary Figure S3. (a) Development of Pt protective coating on the top of the ALD deposited WO_3/TiO_2 heterojunction and filed ion beam (FIB) cut for analysis of interface cross-section. (b) Magnified SEM image identified WO_3/TiO_2 heterojunction. (c) High-magnification FIB-SEM measurement of the WO_3/TiO_2 heterojunction interface. (d) High-resolution TEM observation of the WO_3/TiO_2 heterojunction interface depicts the development of atomic-level ultra-sharp hetero-interfaces between WO_3 and TiO_2 films.

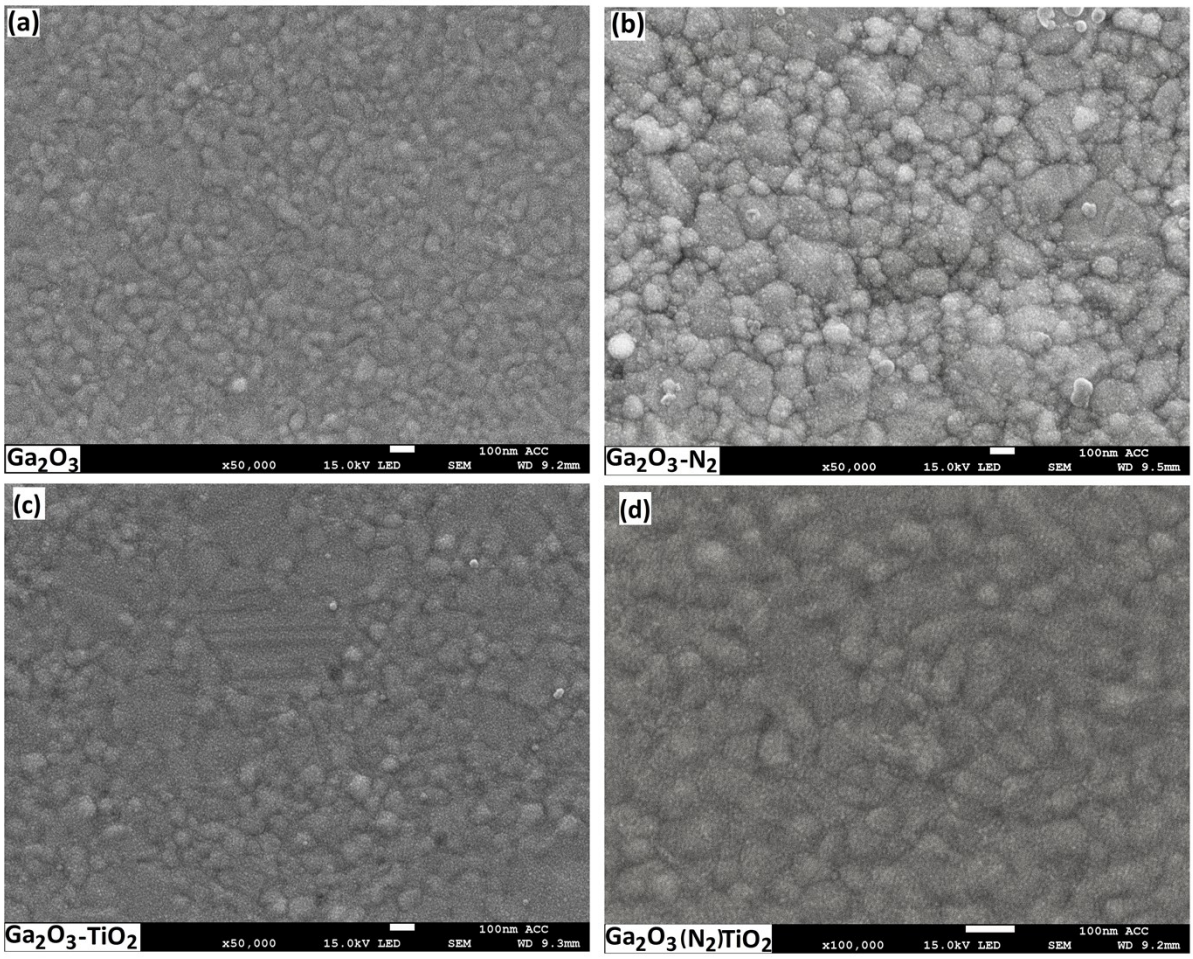

Supplementary Figure S4. (a) The FE-SEM top-view image of surface of as-deposited Ga_2O_3, (b) annealed Ga_2O_3 in N_2 atmosphere, (c) Ga_2O_3-TiO_2, and (d) Ga_2O_3 (N_2)-TiO_2 heterostructured films. The as-deposited Ga_2O_3 film has ultra-fine structure (Supplementary Figure 4a). After annealing in N_2 atmosphere, the grain size of Ga_2O_3 film is slightly increased (supplementary Figure 4b). The SEM observations showed development of uniform TiO_2 films over Ga_2O_3 and Ga_2O_3 (N_2) films.

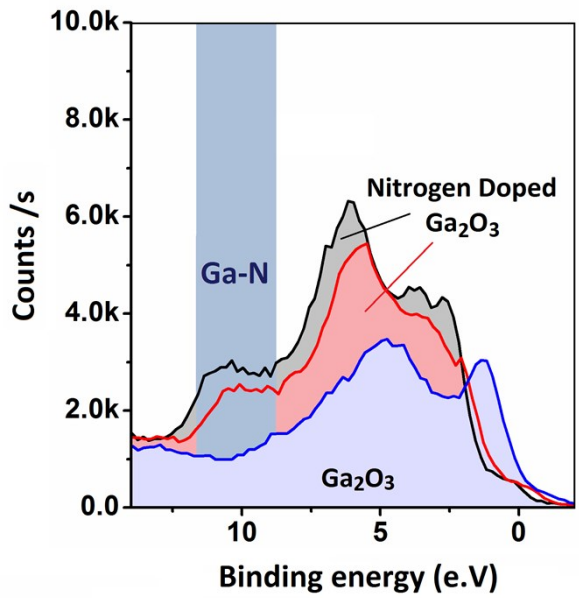

Supplementary Figure S5. The spectrum in ultra-low binding energy region. The characteristics of Ga-N bonding is characterized in Ga_2O_3 films annealed in N_2 atmosphere.

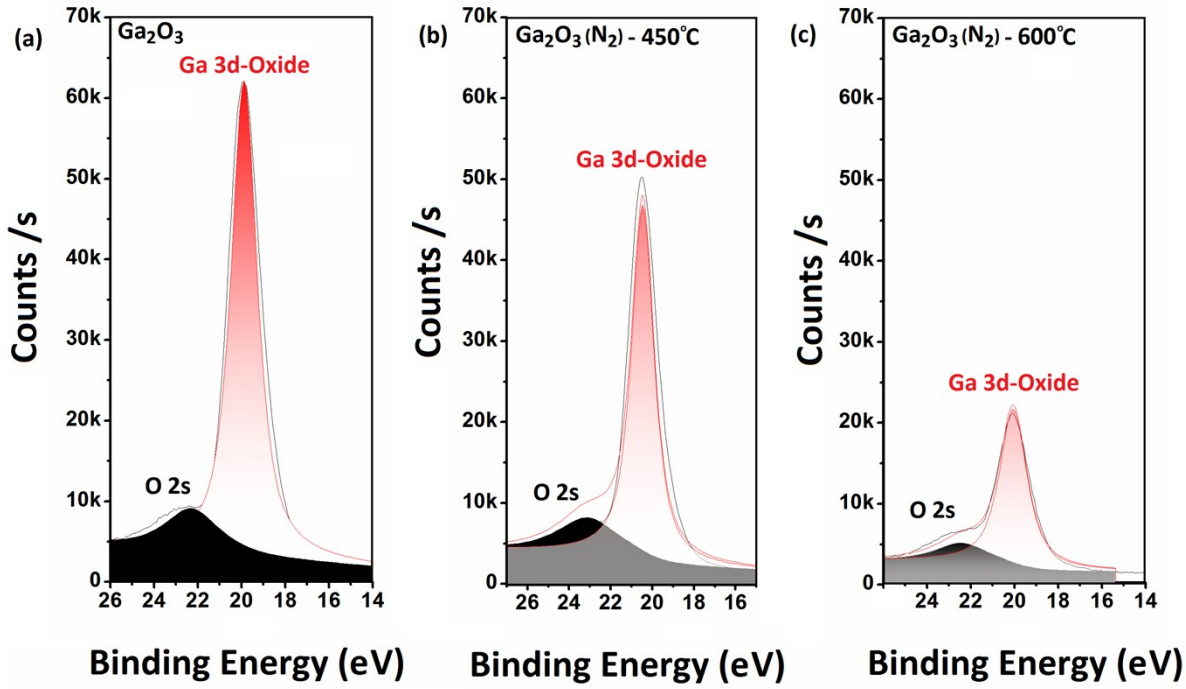

Supplementary Figure S6. The characteristic peaks of Ga-3d in (a) Ga_2O_3, (b) Ga_2O_3 (N_2-450°C) and (c) Ga_2O_3 (N_2-600°C). The intensity of XPS characteristic peak of Ga-O bonding is constantly decreasing after RTA in N_2 atmosphere. It should be mentioned that the tangible decrease of Ga 3d peak of Ga-O bonds happened at the sample annealed at 600°C, an indication of replacement of Ga-N bonding instead of Ga-O bonding.

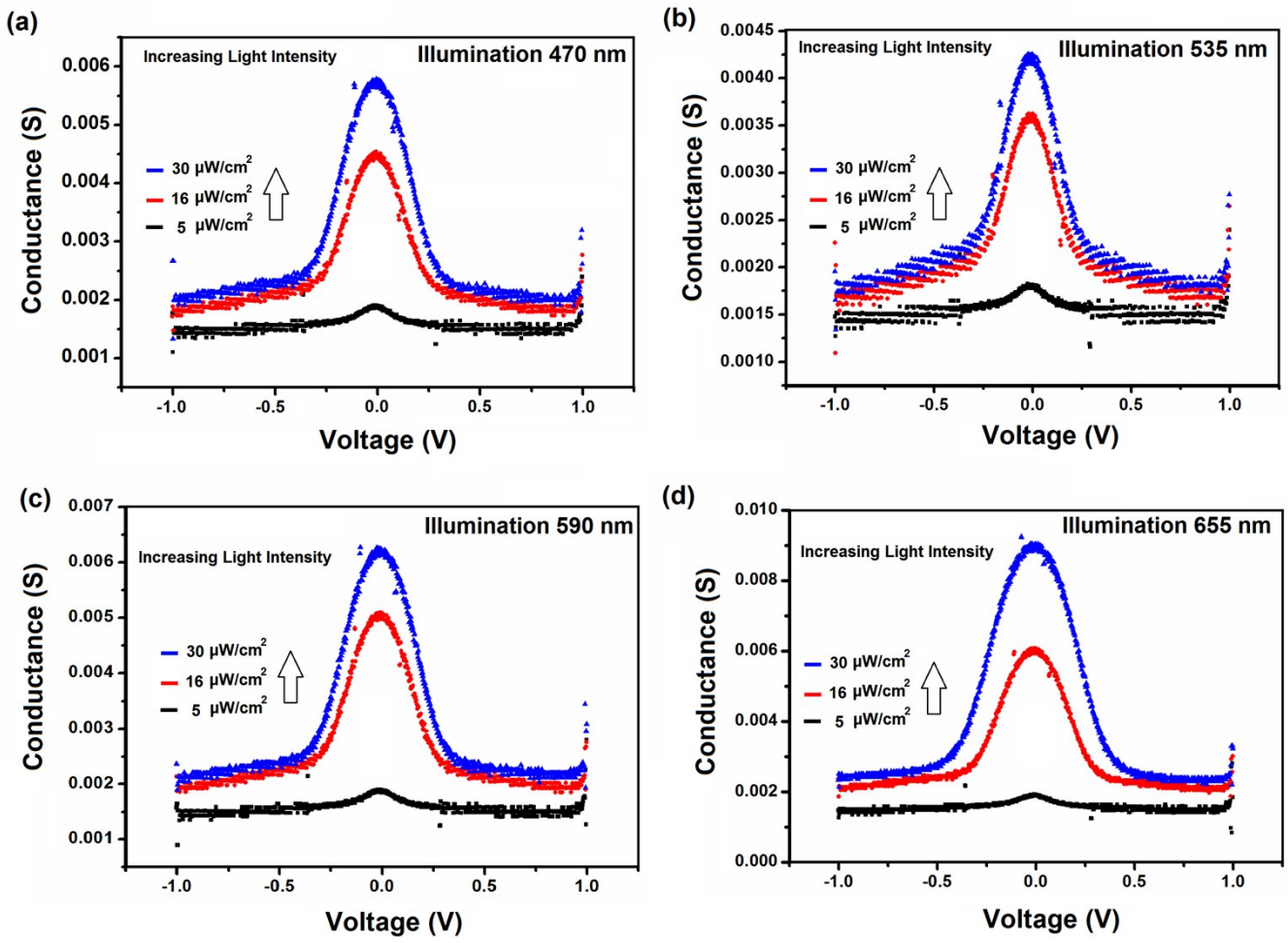

Supplementary Figure S7. Variation of photo-conductance values of Au/Ga_2O_3:TiO_2/ITO devices under illumination of visible LED lights with different wavelengths and intensities.

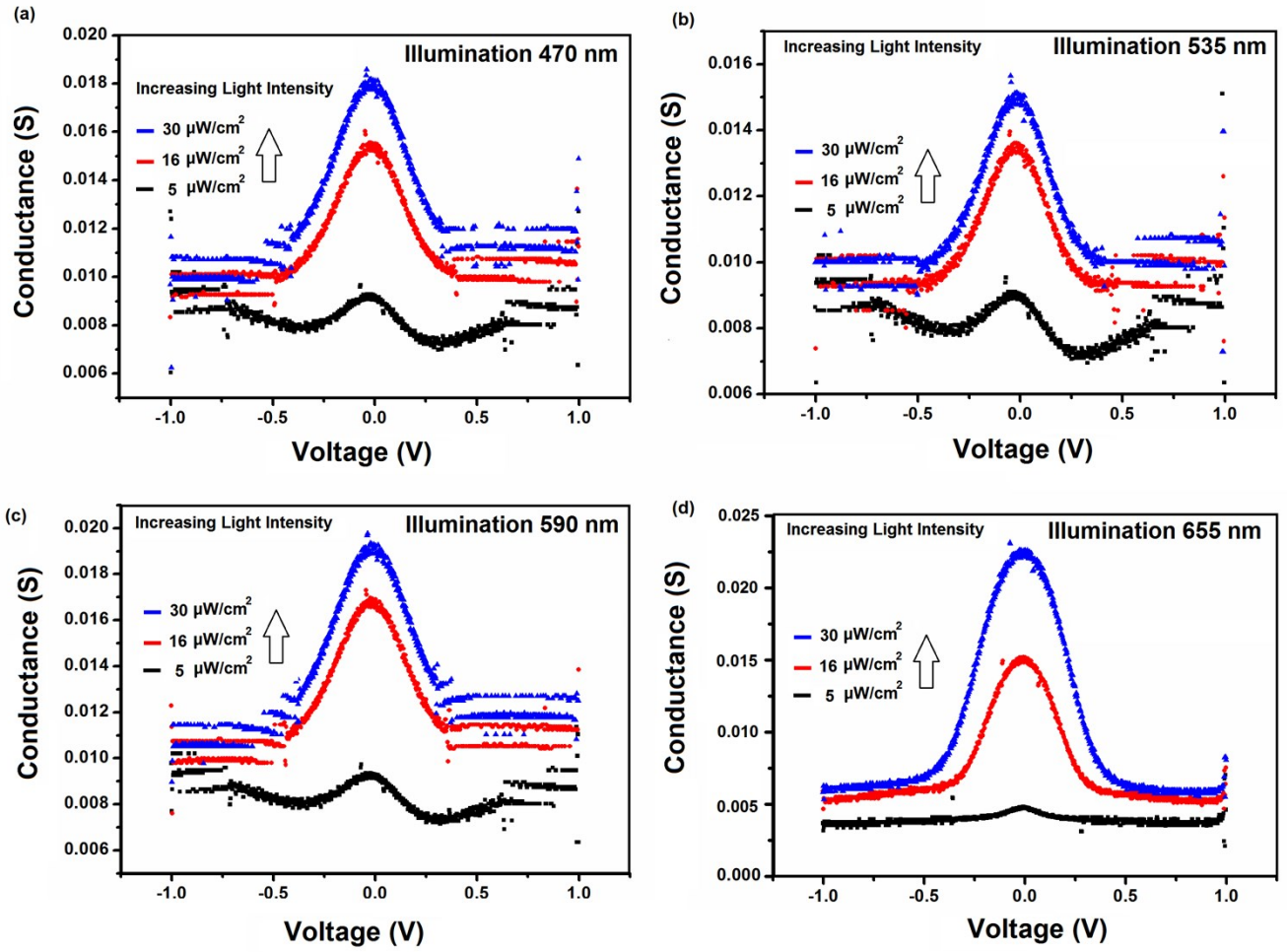

Supplementary Figure S8. Variation of photo-conductance of Au/Ga_2O_3 (N_2):TiO_2/ITO devices under illumination of visible LED lights with different wavelengths and intensities

Supplementary note 1-Calculation of Schottky barrier height

Barrier height of a metal–semiconductor contact can be experimentally measured and determined by using I-V curves. Considering that the current is due to thermionic emission, the relation between the applied forward bias and current can be expressed by[1-4] eq. (1):

$$J = J_0 \exp\left(\frac{qv}{nkt}\right) \tag{1}$$

Where *n* is ideally factor, T is the temperature in Kelvin, *q* is the electron charge, *k* is the Boltzmann constant and I_0 is the reverse saturation current which can be extracted by extrapolation the straight line of lnI to intercept the axis at zero voltage. The Schottky barrier height (SBH) can be calculated by extrapolation of semi-logarithmic *J-V* curves to V=0. The SBH can be calculated from (3):

$$\emptyset_B = \frac{kT}{q} Ln \frac{T^2 A^*}{J_0} \tag{2}$$

$$A^* = \frac{4\pi m^* k^2}{h^3} \tag{3}$$

Where m^* is the effective electron mass, and *h* is the Planck's constant. The A^* is the effective Richardson constant[1-4] which is equal to 54.05 $Acm^{-2}K^{-2}$ for WO_3, 41.1 $Acm^{-2}K^{-2}$ for Ga_2O_3 and 26.4 $Acm^{-2}K^{-2}$ for N_2 doped Ga_2O_3. The experimental *J-V* characteristics and the logarithmic scale of the same graphs are shown in Figure S4-S20. We used low forward bias of *J-V* curves to measure the SBH at Pt/TiO_2 junctions. Taking the logarithmic version of eq. 2, we can extract the *n* and I_0 from the slop and Y axis of *LnJ-V* plot. After performing least square fitting on the *LnJ-V* plot in the linear region, the values of n and J_0 from the slop and the Y-axis can be determined.

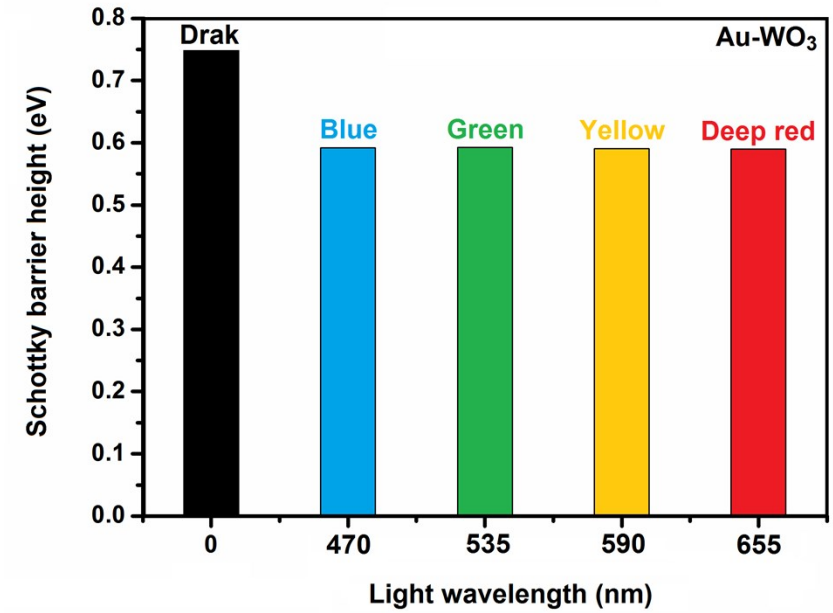

Supplementary Figure S9. The variation of Schottky barrier height at Au/WO_2 at different light wavelengths.

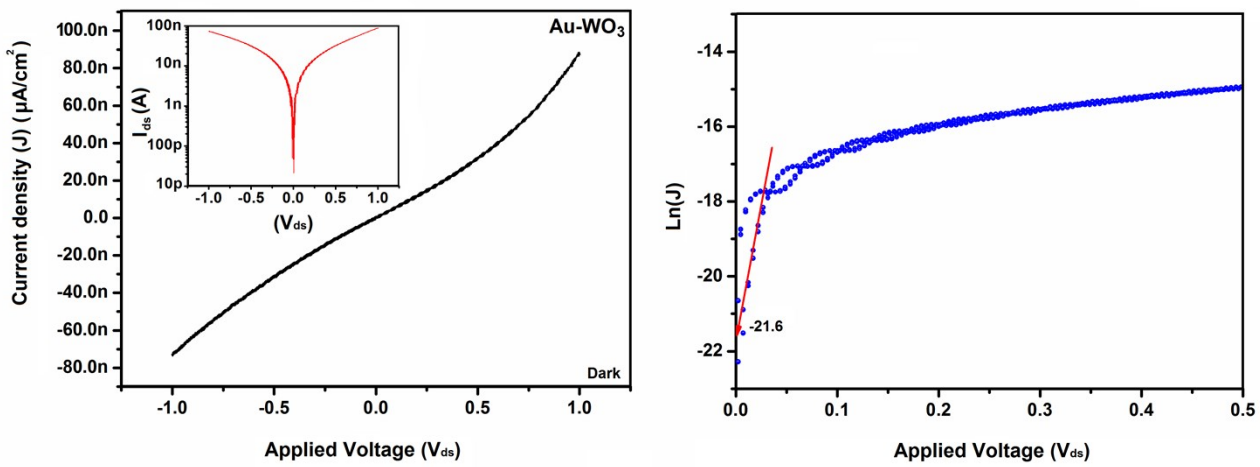

Supplementary Figure S10. The *J*-V_{ds} characteristics of Au/WO_3 device and Ln*J*-*V* plot of the Au/WO_3 junction (Schottky diode) at the 273K and under dark condition.

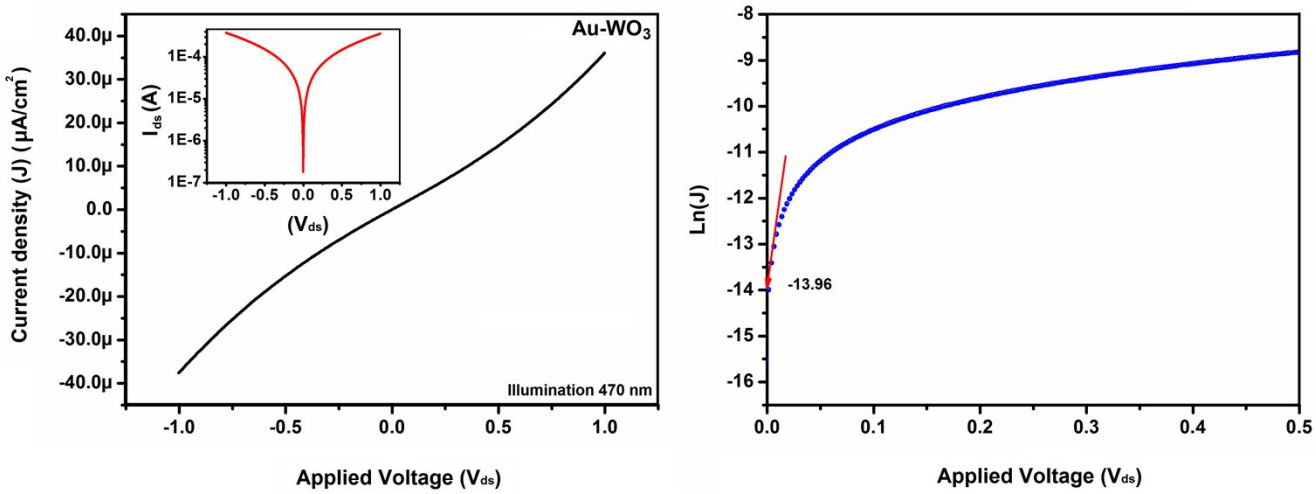

Supplementary Figure S11. The *J*-V_{ds} characteristics of Au/WO_3 device and Ln*J*-*V* plot of the Au/WO_3 junction (Schottky diode) at the 273K under and λ= 470 nm illumination.

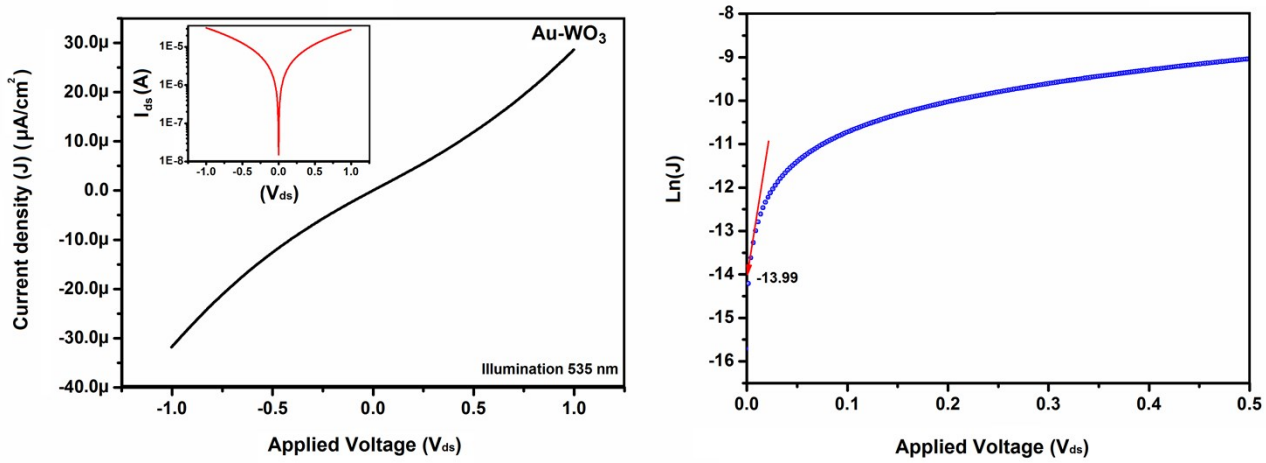

Supplementary Figure S12. The *J*-V_{ds} characteristics of Au/WO_3 device and Ln*J*-*V* plot of the Au/WO_3 junction (Schottky diode) at the 273K and under λ= 535 nm illumination.

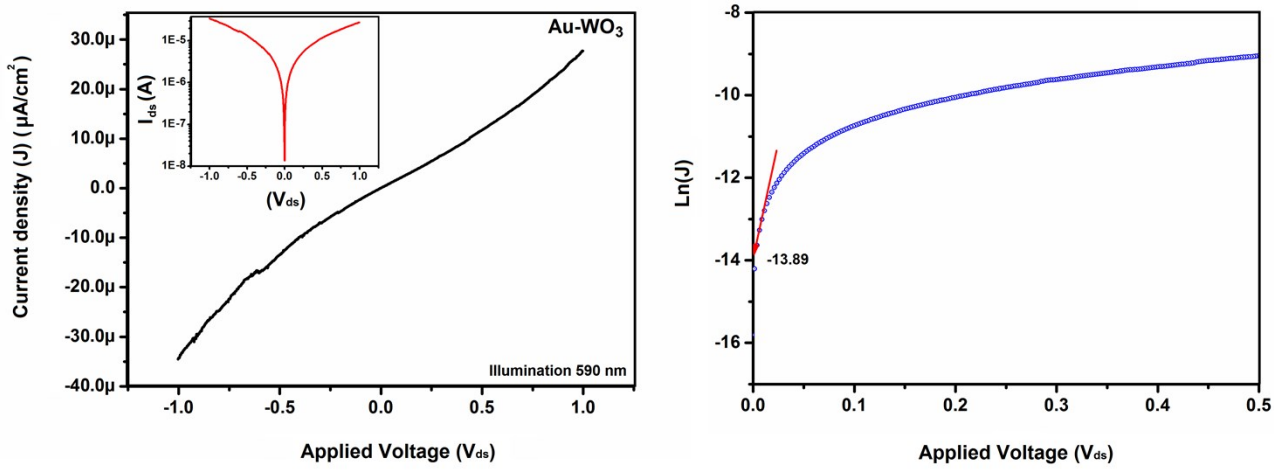

Supplementary Figure S13. The *J*-V_{ds} characteristics of Au/WO_3 device and Ln*J*-*V* plot of the Au/WO_3 junction (Schottky diode) at the 273K and under λ= 590 nm illumination.

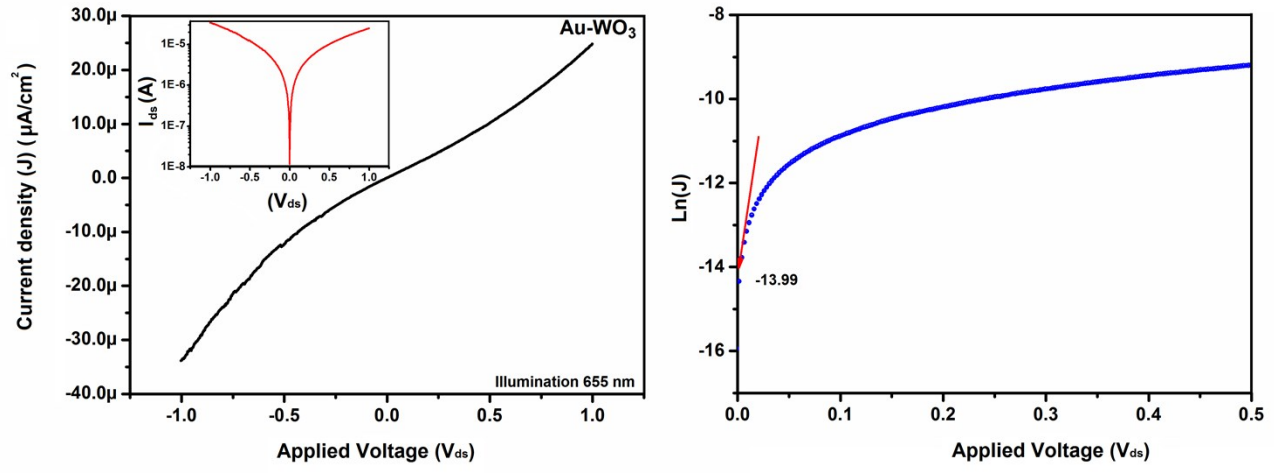

Supplementary Figure S14. The *J*-V_{ds} characteristics of Au/WO_3 device and Ln*J*-*V* plot of the Au/WO_3 junction (Schottky diode) at the 273K and under λ= 655 nm illumination.

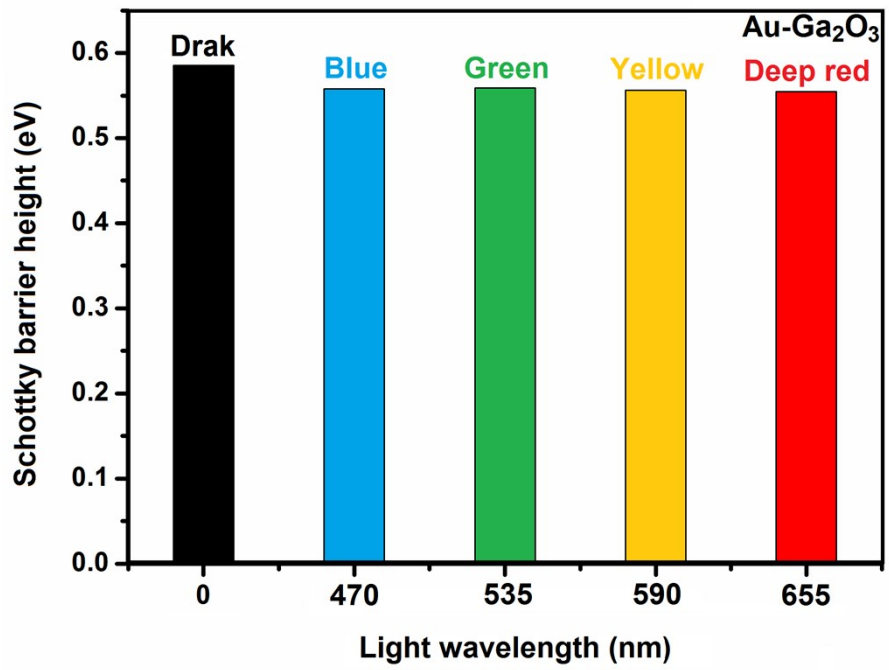

Supplementary Figure S15. The variation of Schottky barrier height at Au/Ga_2O_3 at different light wavelengths.

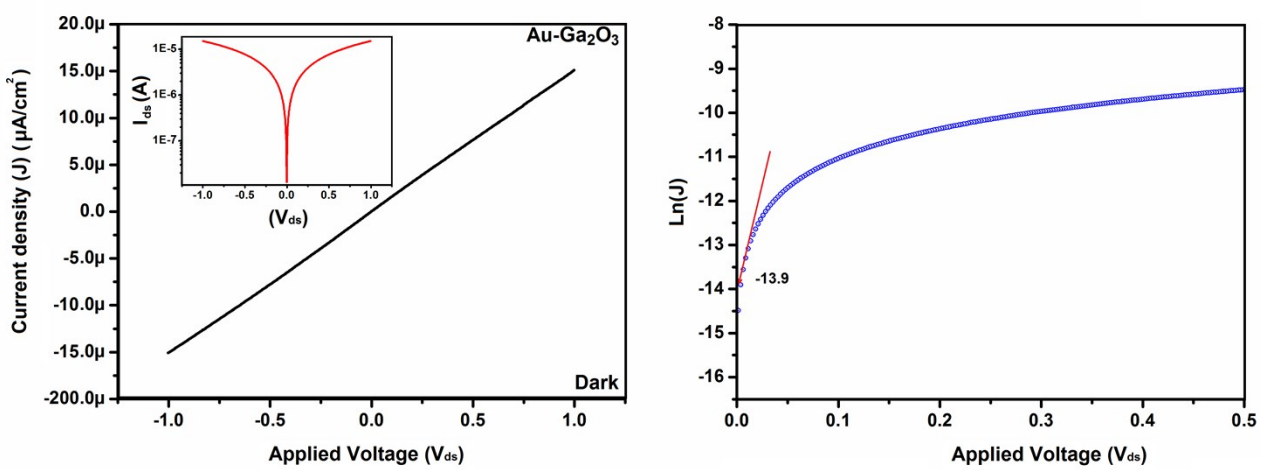

Supplementary Figure S16. The *J*-V_{ds} characteristics of Au/Ga_2O_3 device and Ln*J*-*V* plot of the Au/WO_3 junction (Schottky diode) at the 273K and under dark condition.

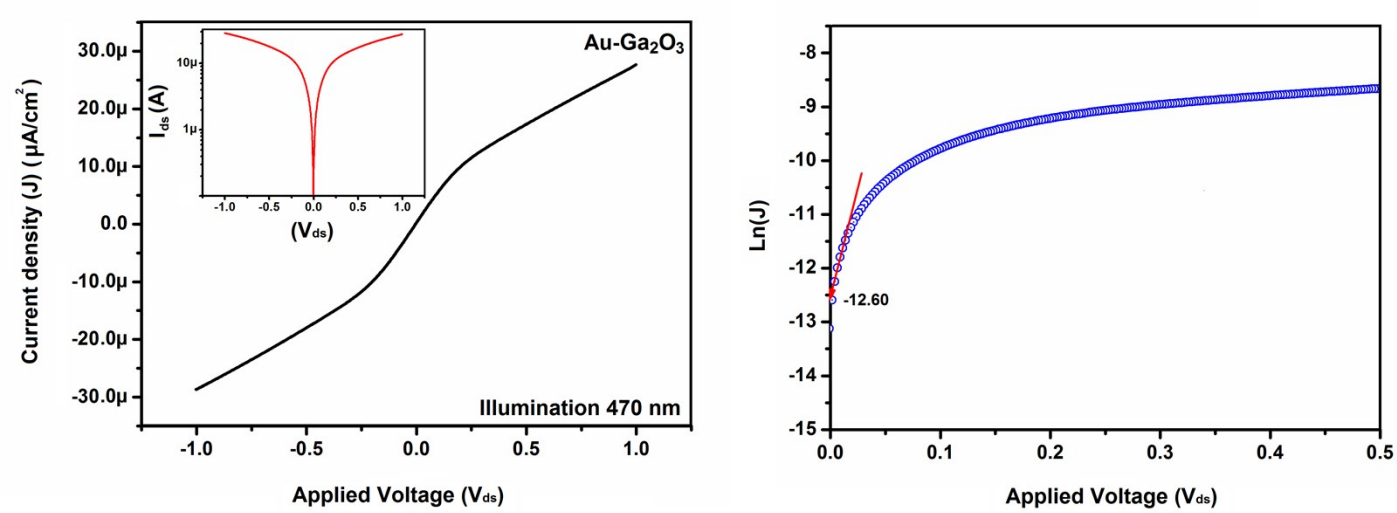

Supplementary Figure S17. The *J*-V_{ds} characteristics of Au/Ga_2O_3 device and LnJ-V plot of the Au/Ga_2O_3 junction (Schottky diode) at the 273K and under λ= 470 nm illumination.

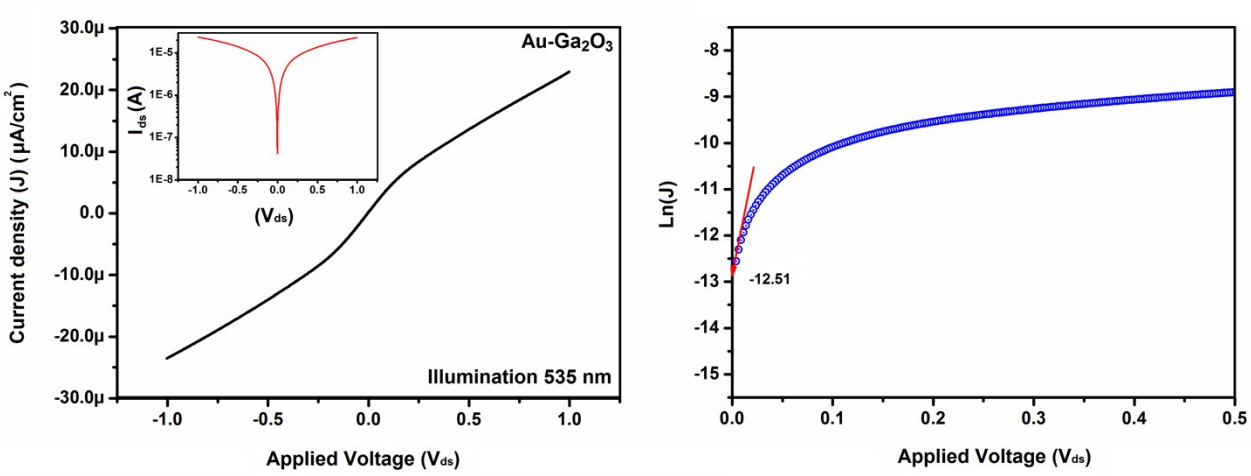

Supplementary Figure S18. The *J*-V_{ds} characteristics of Au/Ga_2O_3 device and Ln*J*-*V* plot of the Au/Ga_2O_3 junction (Schottky diode) at the 273K and under λ= 535 nm illumination.

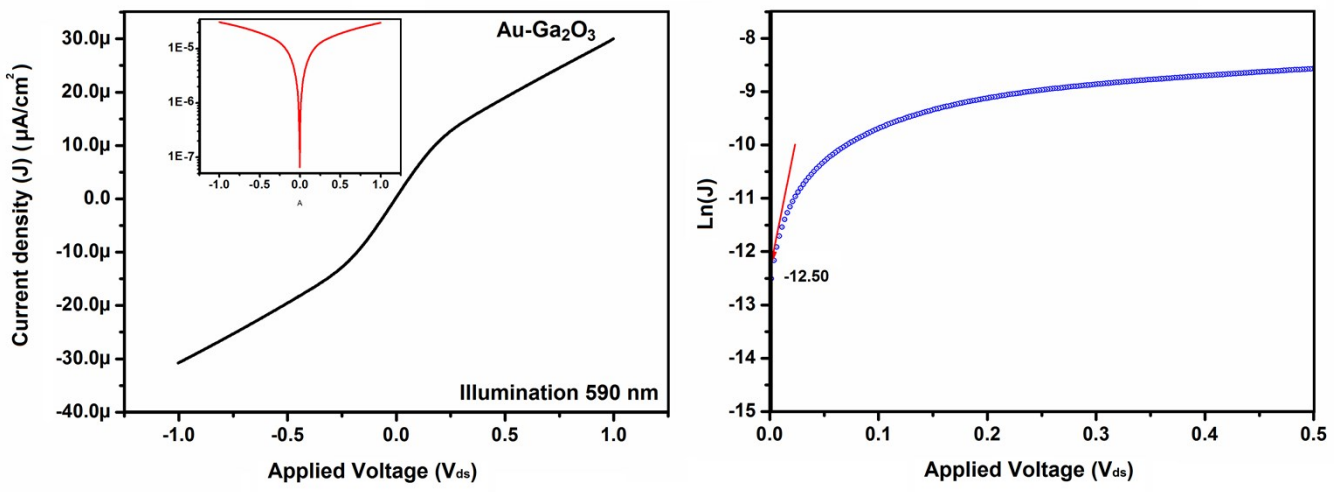

Supplementary Figure S19. The *J*-V_{ds} characteristics of Au/Ga_2O_3 device and (b) Ln*J*-*V* plot of the Au/Ga_2O_3 junction (Schottky diode) at the 273K and under λ= 590 nm illumination.

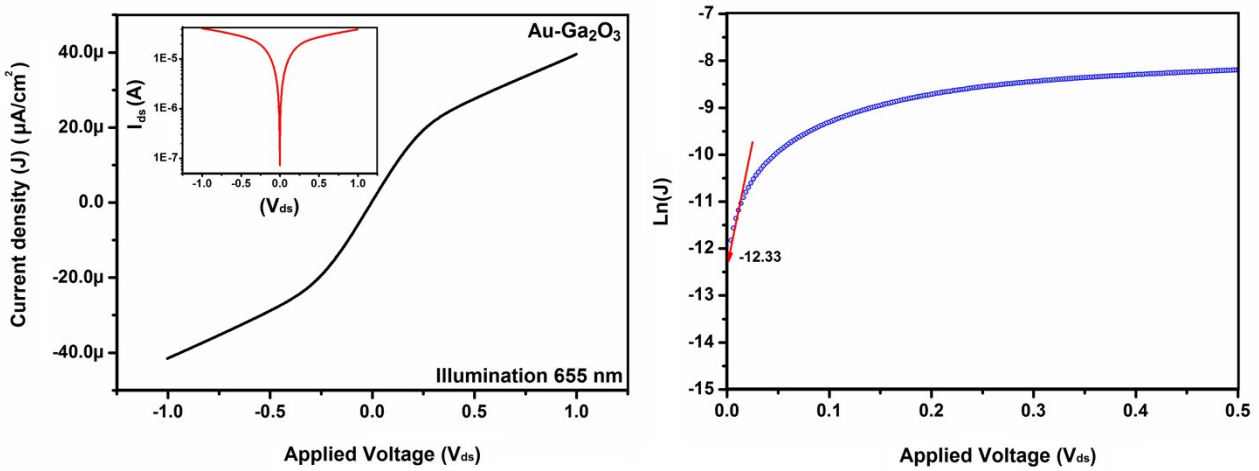

Supplementary Figure S20. The *J*-V_{ds} characteristics of Au/Ga_2O_3 device and Ln*J*-*V* plot of the Au/Ga_2O_3 junction (Schottky diode) at the 273K and under λ= 655 nm illumination.

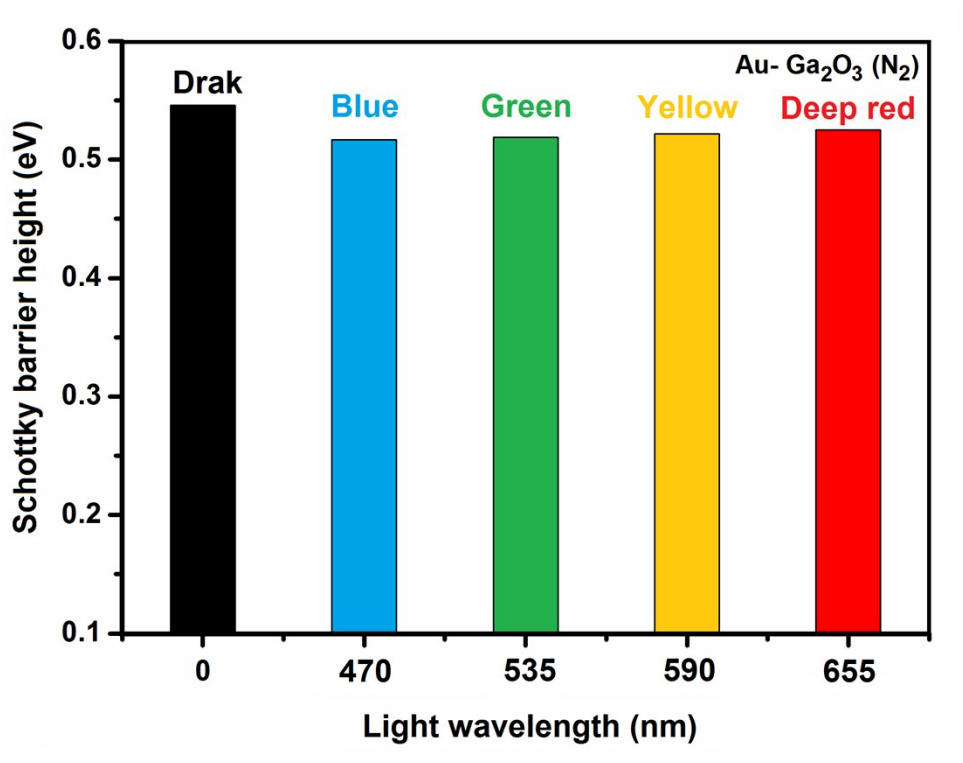

Supplementary Figure S21. The variation of Schottky barrier height at Au/Ga_2O_3 (N_2) at different light wavelengths.

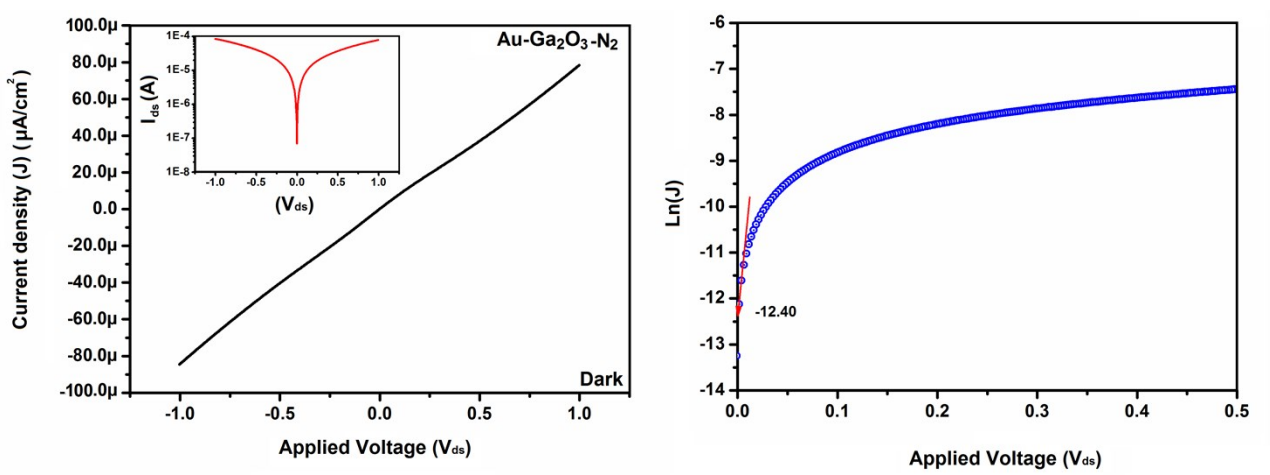

Supplementary Figure S22. The *J*-V_{ds} characteristics of Au/Ga_2O_3 (N_2) device and Ln*J*-*V* plot of the Au/Ga_2O_3 junction (Schottky diode) at the 273K under and dark condition.

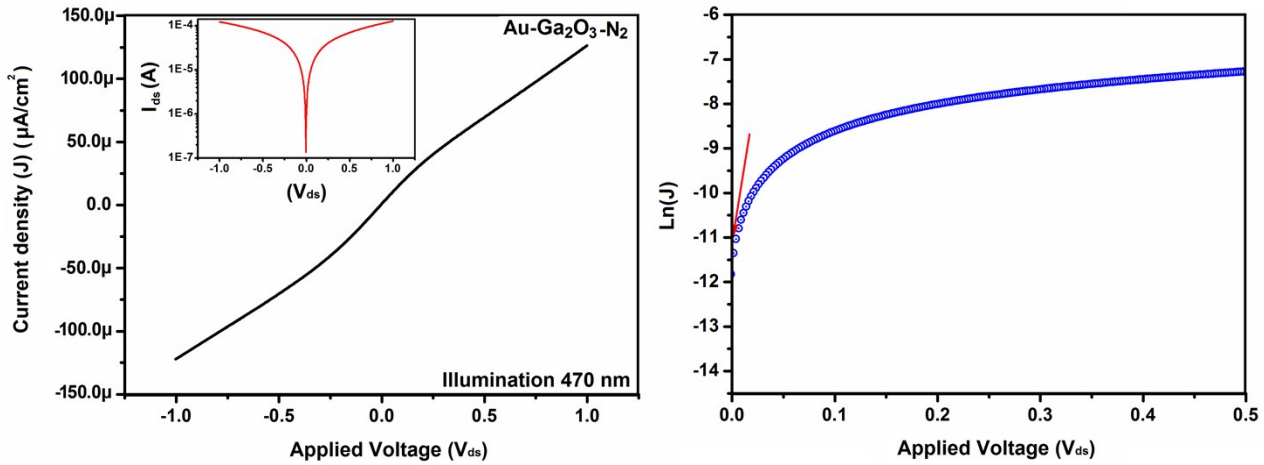

Supplementary Figure S23. The *J*-V_{ds} characteristics of Au/Ga_2O_3 (N_2) device and Ln *J*-*V* plot of the Au/Ga_2O_3 junction (Schottky diode) at the 273K and under λ= 470 nm illumination.

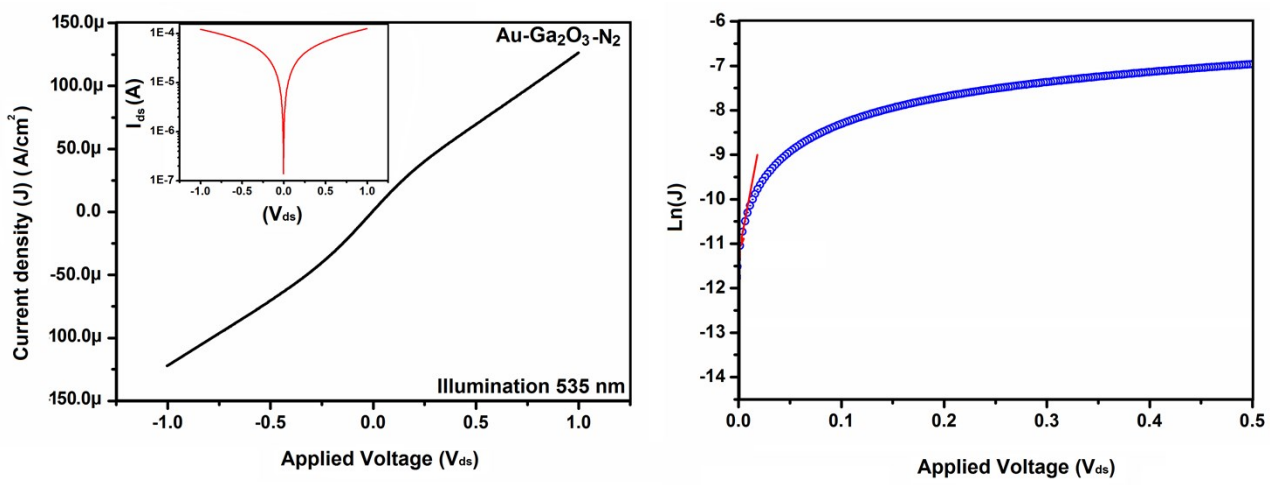

Supplementary Figure S24. The *J*-V_{ds} characteristics of Au/Ga_2O_3 (N_2) device and Ln*J*-*V* plot of the Au/Ga_2O_3 junction (Schottky diode) at the 273K and under λ= 535 nm illumination.

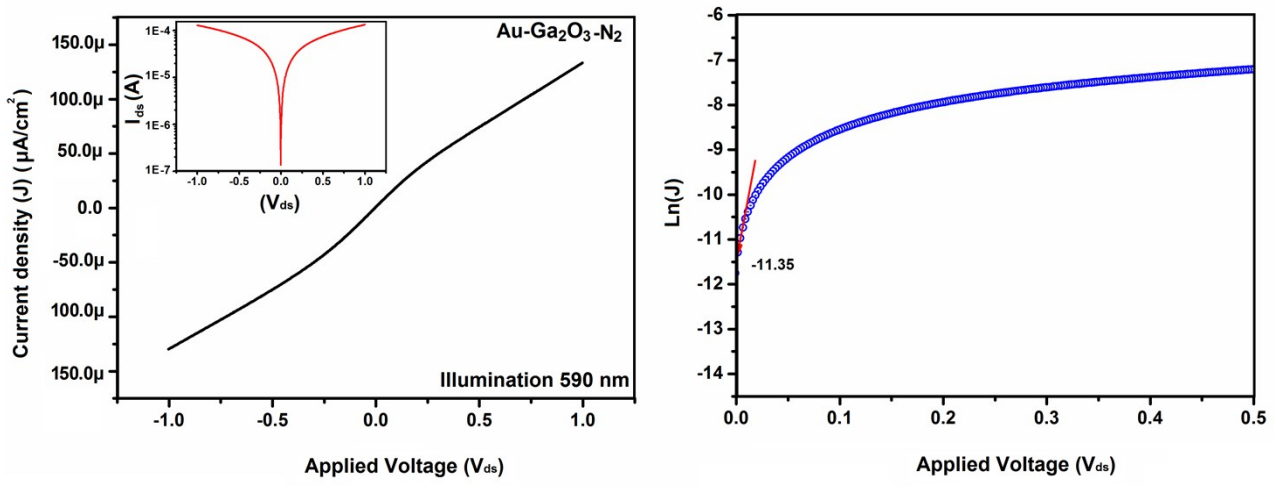

Supplementary Figure S25. The *J*-V_{ds} characteristics of Au/Ga_2O_3 (N_2) device and Ln *J*-*V* plot of the Au/Ga_2O_3 junction (Schottky diode) at the 273K and under λ= 590 nm illumination.

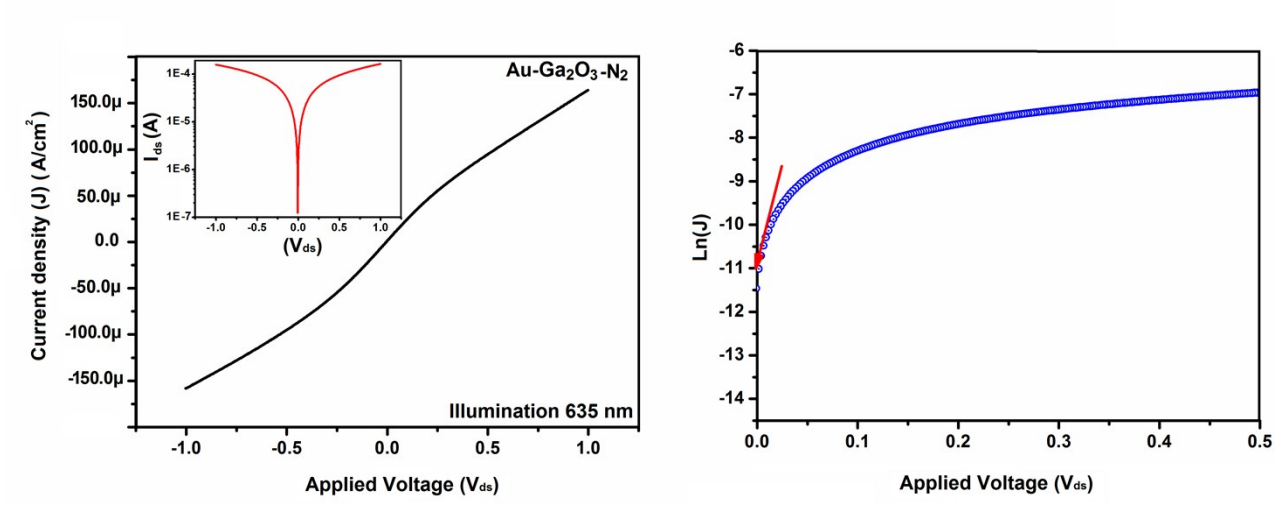

Supplementary Figure S26. The *J*-V_{ds} characteristics of Au/Ga_2O_3 (N_2) device and Ln *J*-*V* plot of the Au/Ga_2O_3 junction (Schottky diode) at the 273K and under λ= 635 nm illumination.

Supplementary note 2: Band alignment calculation at WO_3-TiO_2 and Ga_2O_3-TiO_2 heterostructure

Based on Kraut's method, the valence band offset (VBO) can be extracted by following formula[5,6]:

$$\Delta E_V = \left(E_{W\,4F}^{WO_3} - E_{VBM}^{WO_3}\right) - \left(E_{Ti\,2P}^{TiO_2} - E_{VBM}^{TiO_2}\right) - \left(E_{W\,4F}^{WO_3} - E_{Ti\,2P}^{TiO_2}\right) \quad (4)$$

$$\Delta E_V = \left(E_{Ga\,2P}^{Ga_2O_3} - E_{VBM}^{Ga_2O_3}\right) - \left(E_{Ti\,2P}^{TiO_2} - E_{VBM}^{TiO_2}\right) - \left(E_{Ga\,2P}^{Ga_2O_3} - E_{Ti\,2P}^{TiO_2}\right) \quad (5)$$

$$\Delta E_V = \left(E_{Ga\,2P}^{Ga_2O_3(N2)} - E_{VBM}^{Ga_2O_3\,(N2)}\right) - \left(E_{Ti\,2P}^{TiO_2} - E_{VBM}^{TiO_2}\right) - \left(E_{Ga\,2P}^{Ga_2O_3\,(N2)} - E_{Ti\,2P}^{TiO_2}\right) \quad (6)$$

In which, $E_{W\,4F}^{WO_3}$ is core level (CL) spectra of W 4F, $E_{VBM}^{WO_3}$ is the valence band maximum (VBM) of WO_3. $E_{Ga\,2P}^{Ga_2O_3}$ is core level (CL) spectra of Ga 2p, $E_{VBM}^{Ga_2O_3}$ is the valence band maximum (VBM) of Ga_2O_3, $E_{Ti\,2P}^{TiO_2}$ is the CL of Ti 2P spectra, $E_{VBM}^{TiO_2}$ is the VBM of TiO_2. To calculate the VBM of WO_3, Ga_2O_3, Ga_2O_3 (N_2) and TiO_2, the XPS spectra of WO_3-TiO_2, Ga_2O_3-TiO_2, Ga_2O_3 (N_2)-TiO_2 were used (Supplementary Figure S27-S29). To describe the integrated band offsets of WO_3-TiO_2, Ga_2O_3-TiO_2, Ga_2O_3 (N_2)-TiO_2 heterojunctions, the corresponding energy difference between conduction bands can be calculated from Formula (7, 8 and 9):

$$\Delta E_C = E_{Bandgap}^{WO_3} - E_{Bandgap}^{TiO_2} - \Delta E_V \quad (7)$$

$$\Delta E_C = E_{Bandgap}^{Ga_2O_3} - E_{Bandgap}^{TiO_2} - \Delta E_V \quad (8)$$

$$\Delta E_C = E_{Bandgap}^{Ga_2O_3(N2)} - E_{Bandgap}^{TiO_2} - \Delta E_V \quad (9)$$

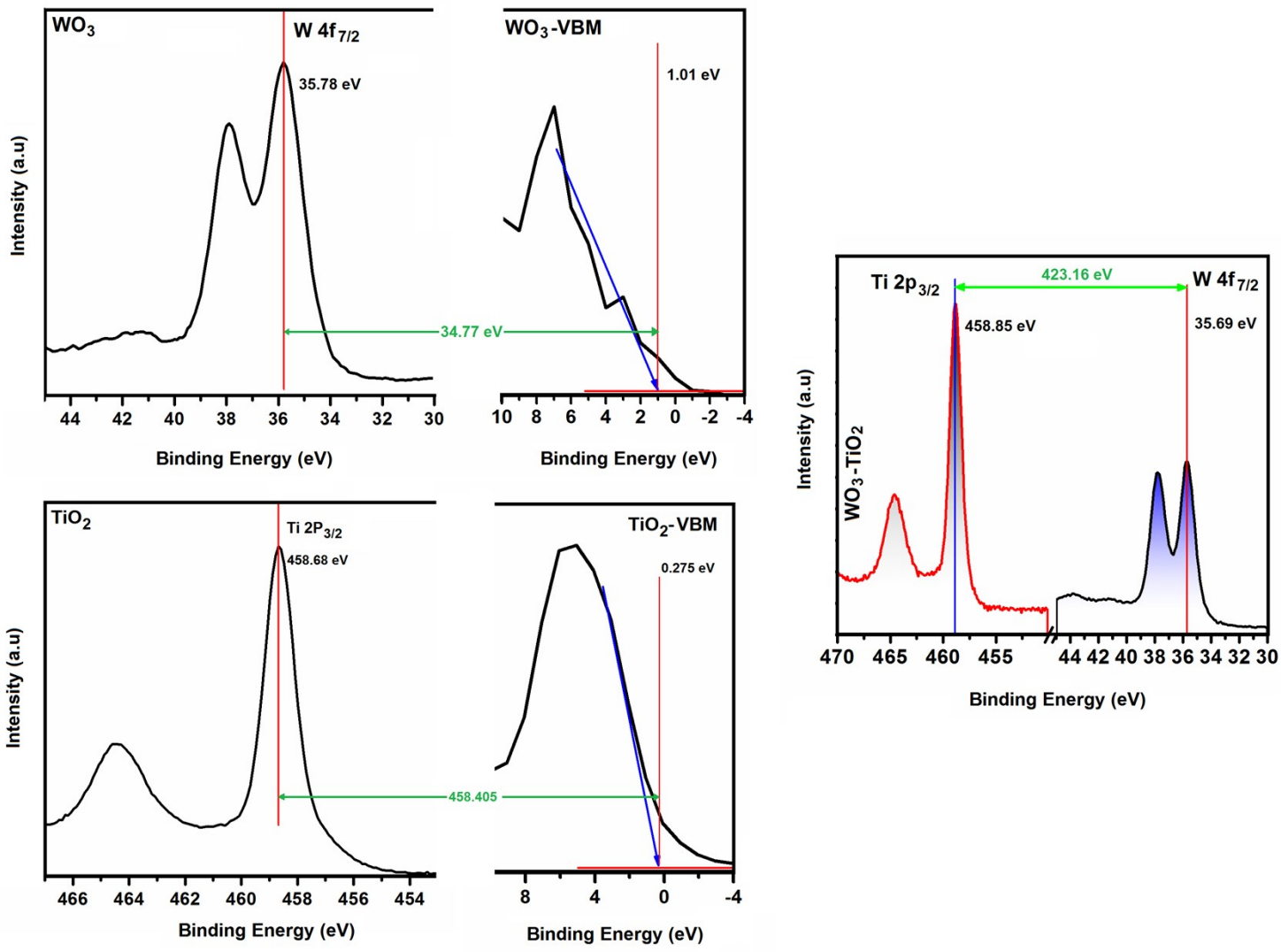

Supplementary Figure S27. Parameters for calculation of energy band alignment at WO_3-TiO_2 heterostructures.

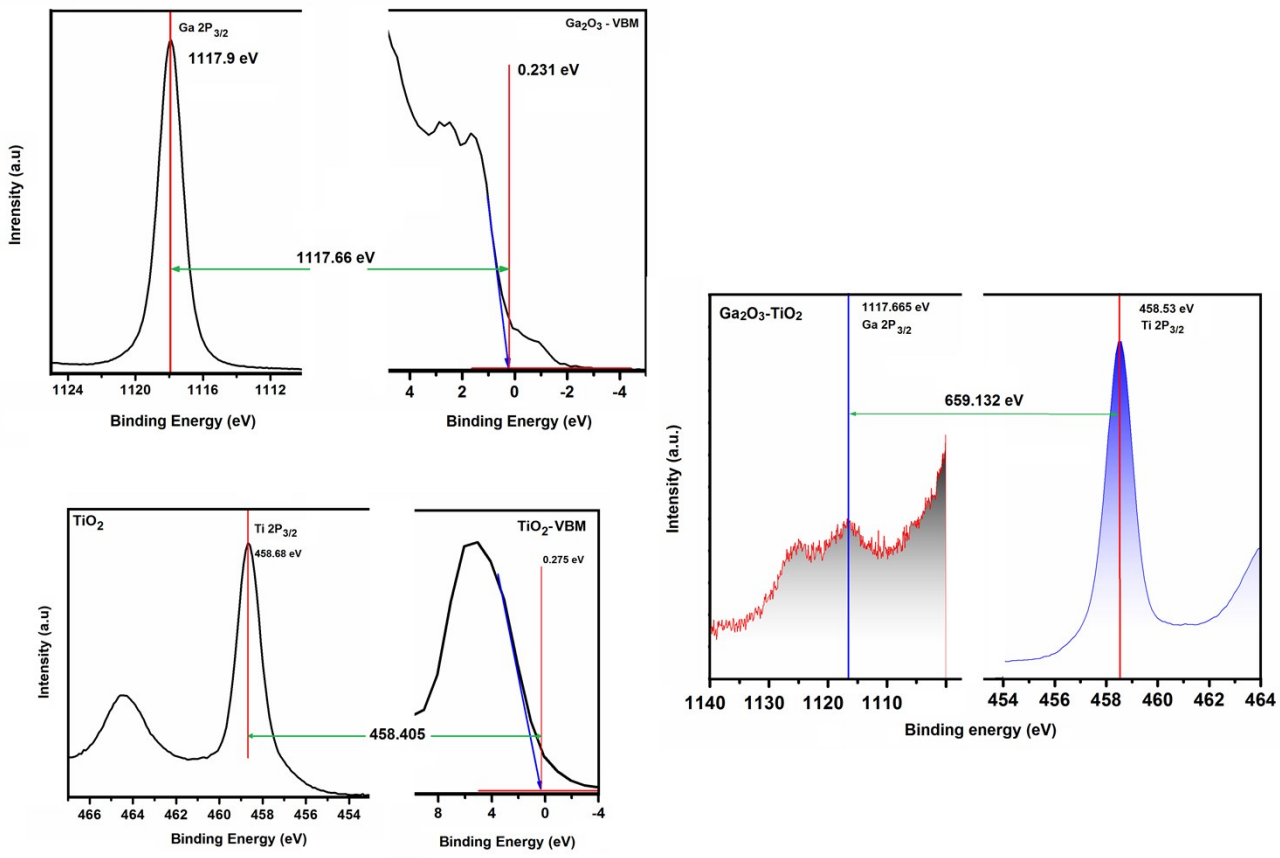

Supplementary Figure S28. Parameters for calculation of energy band alignment at Ga_2O_3-TiO_2 heterostructures.

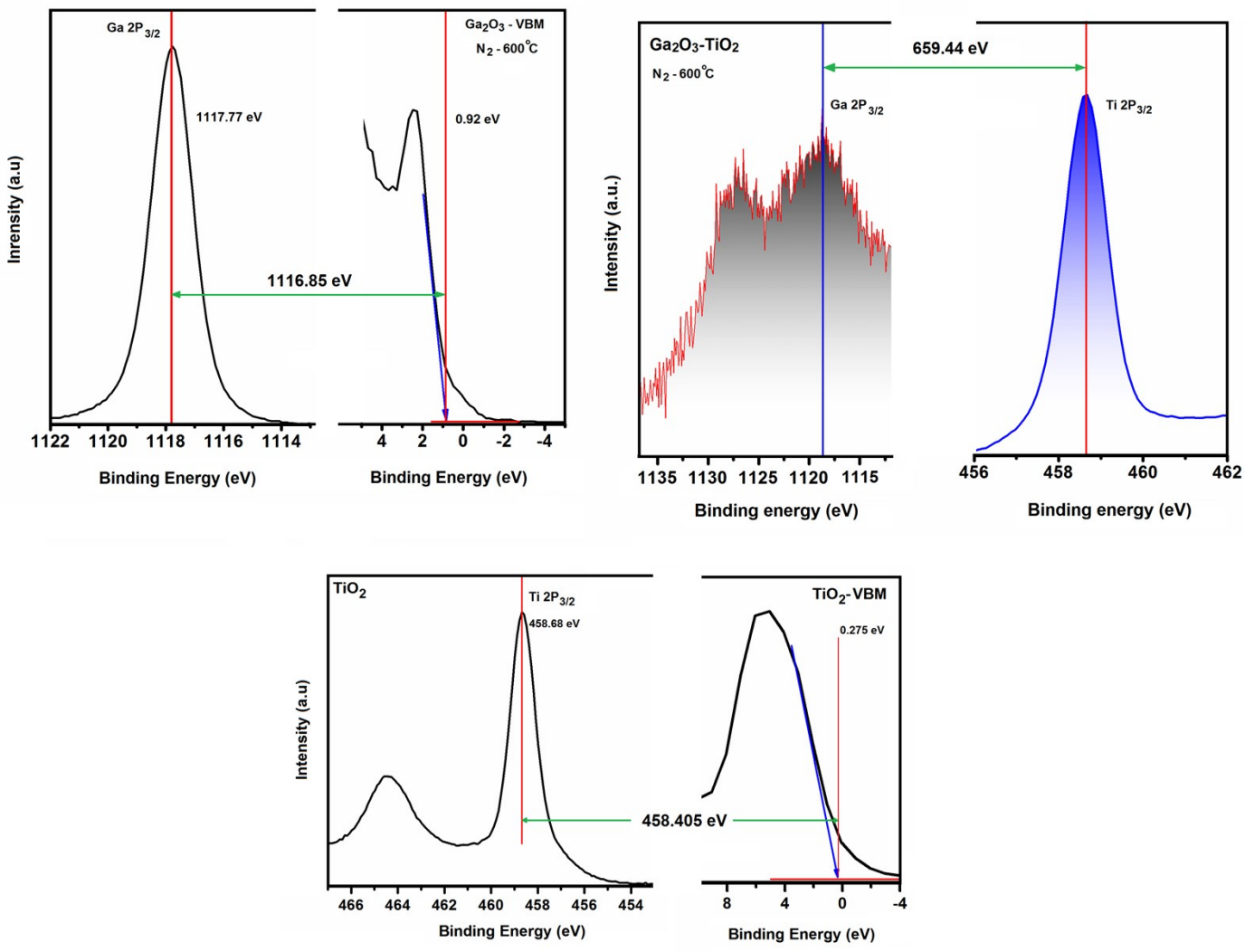

Supplementary Figure S29. Parameters for calculation of energy band alignment at Ga_2O_3 (N_2)-TiO_2 heterostructures.

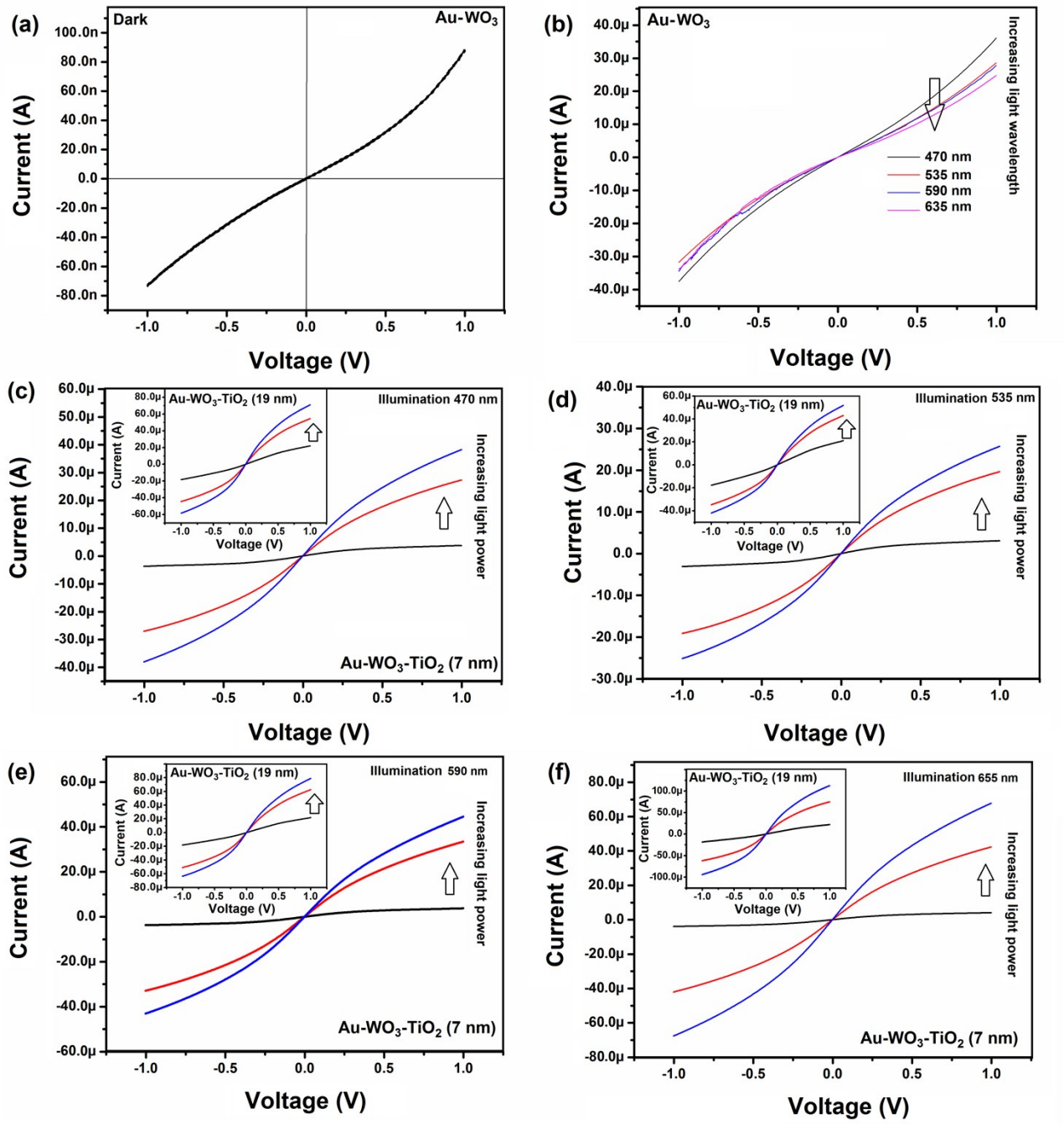

Supplementary Figure S30. Photocurrent variation of WO_3 and WO_3-TiO_2 heterostructured device at different light wavelengths, various light intensities and different TiO_2 thicknesses (7 nm and 19 nm).

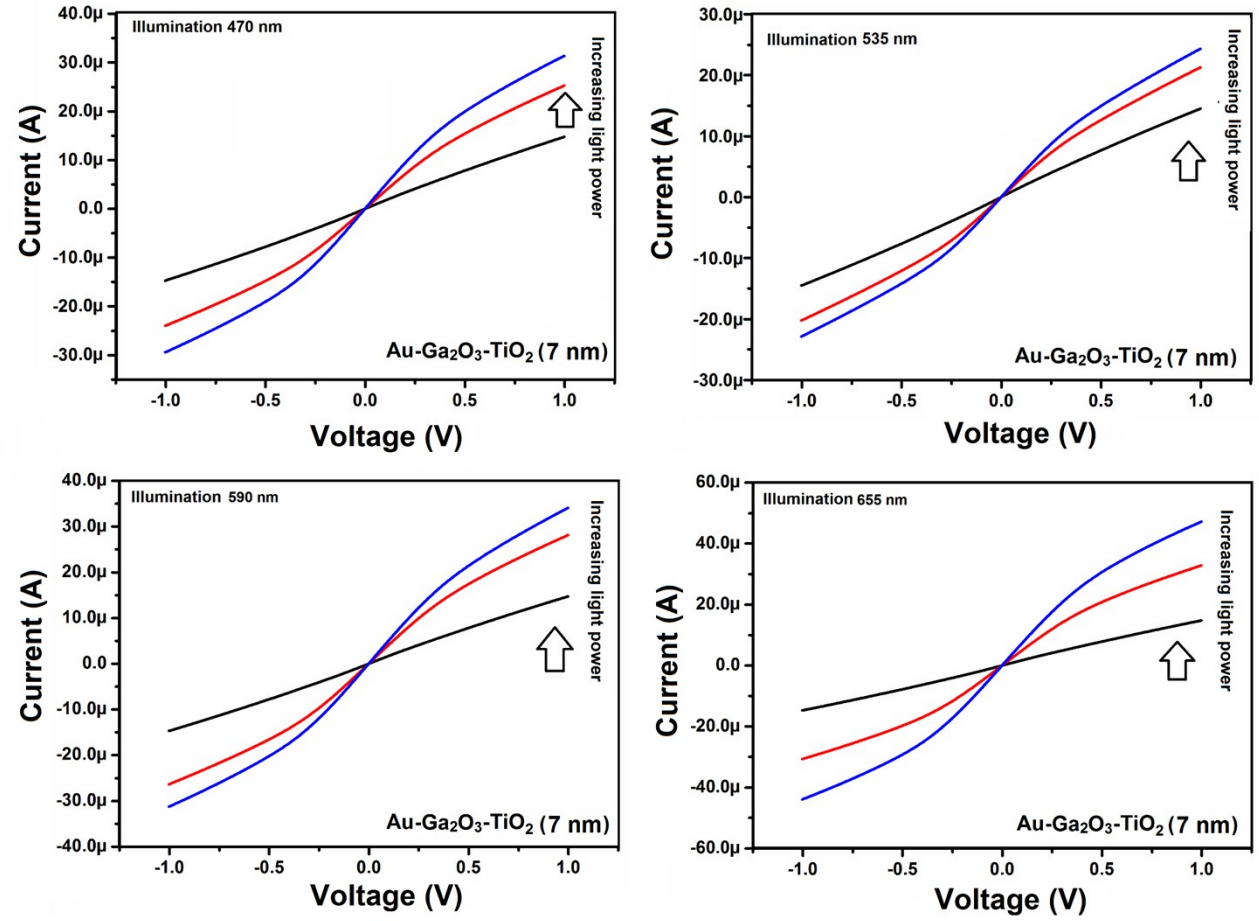

Supplementary Figure S31. Photocurrent variation of Ga_2O_3-TiO_2 (7 nm) heterostructured device at different light wavelengths, and various light intensities.

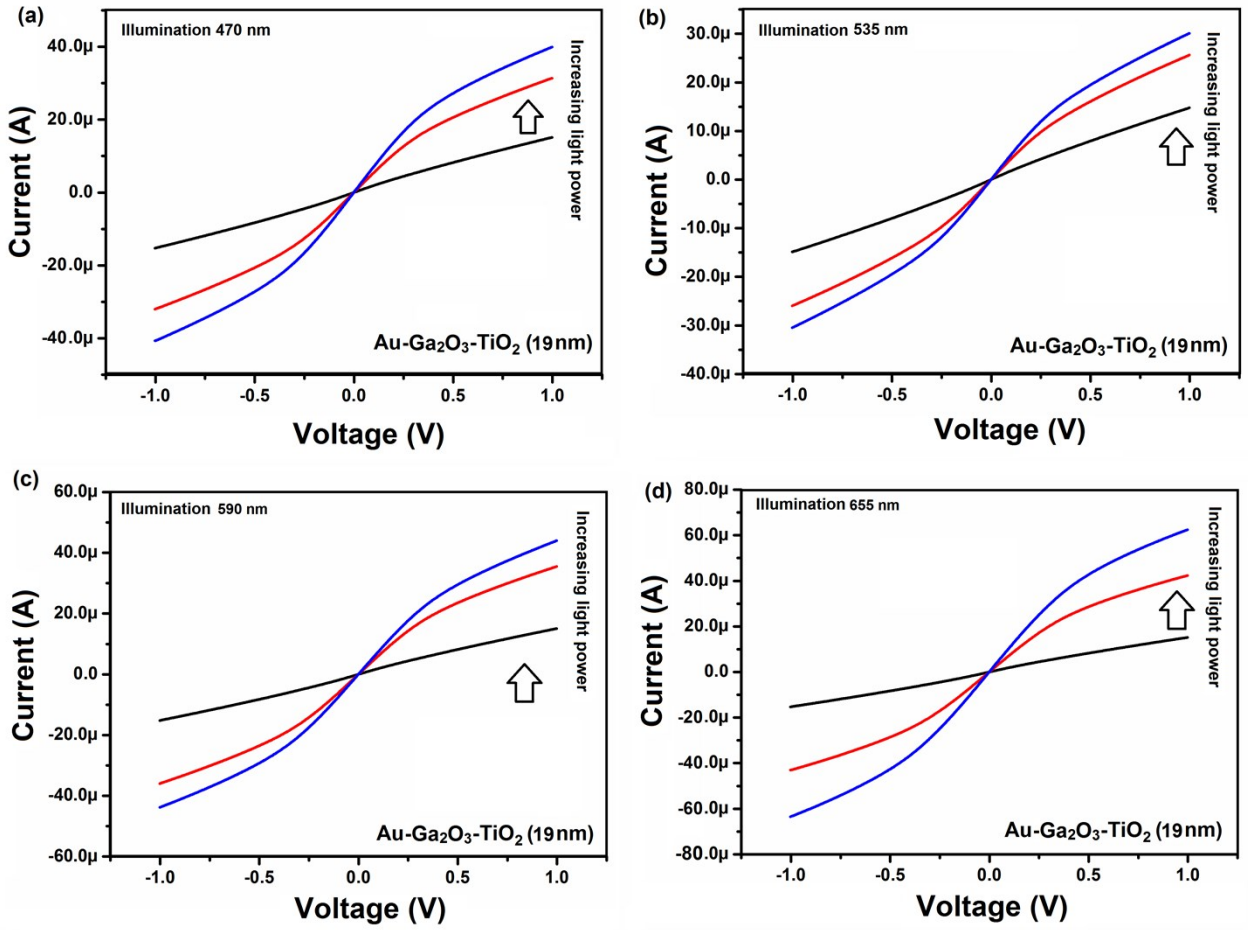

Supplementary Figure S32. Photocurrent variation of Ga_2O_3-TiO_2 (19 nm) heterostructured device at different light wavelengths, and various light intensities.

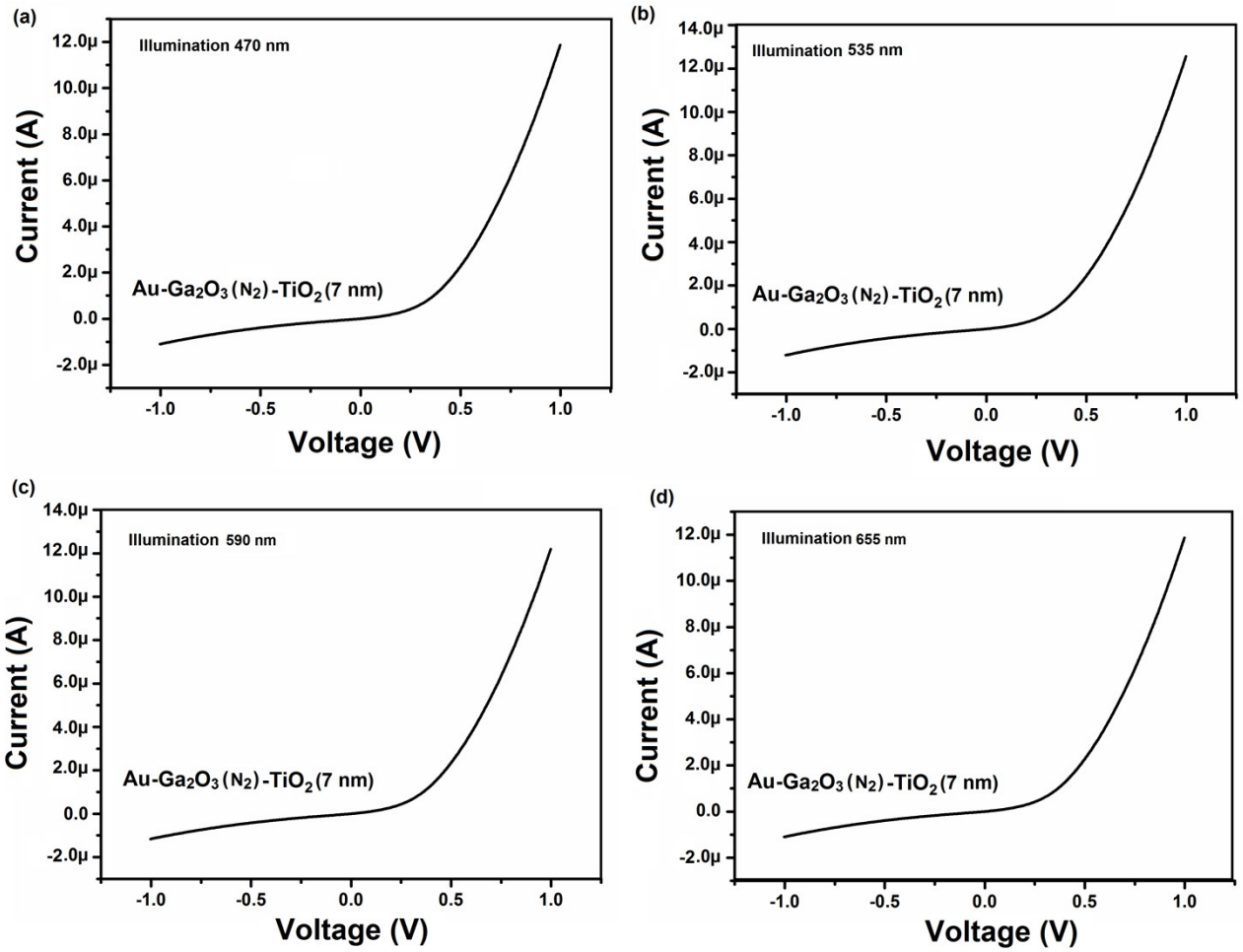

Supplementary Figure S33. Photocurrent variation of Ga_2O_3 (N_2)-TiO_2 (7 nm) heterostructured device at different light wavelengths.

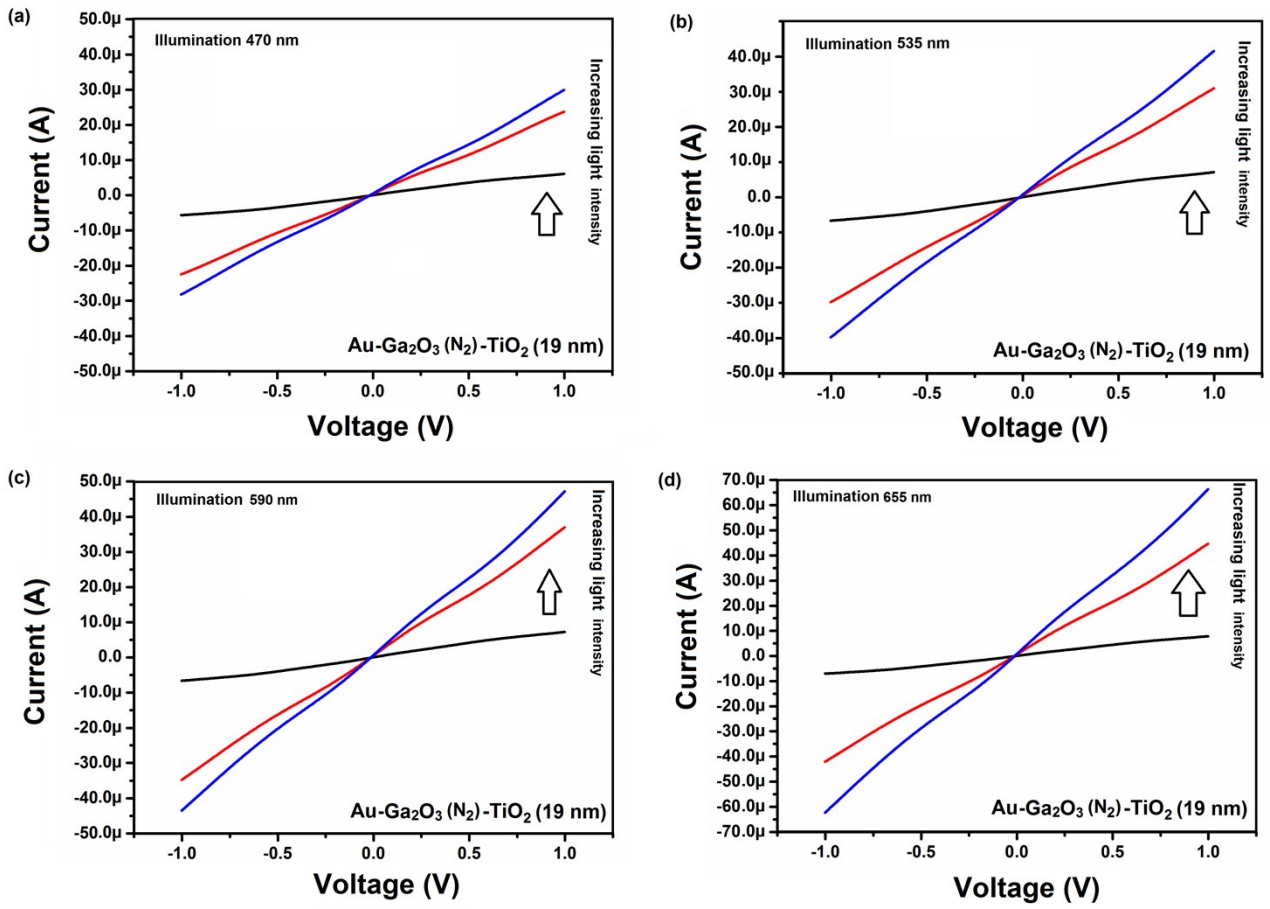

Supplementary Figure S34. Photocurrent variation of Ga_2O_3 (N_2)-TiO_2 (19 nm) heterostructured device at different light wavelengths, and various light intensities.

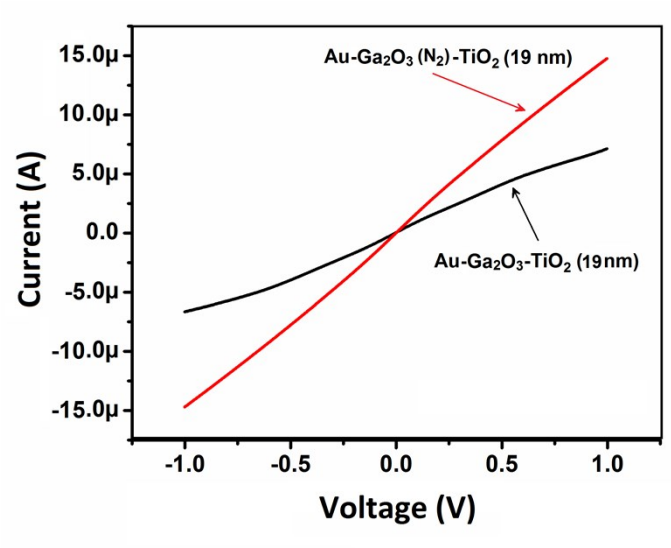

Supplementary Figure S35. Variation of dark current of Ga_2O_3-TiO_2 (19 nm) and Ga_2O_3 (N_2)-TiO_2 based devices which were employed as nociceptive devices.

Table S1: The characteristics of receptors f presented study for λ= 655 nm light with the power density of 25 µw/cm^2.

Device	Photoresponsivity	EQE
WO_3-TiO_2	0.4 mA/W	6.28 %
Ga_2O_3-TiO_2	1.8 mA/W	28.2%
Ga_2O_3 (N_2)-TiO_2	3.6 mA/W	56.5%

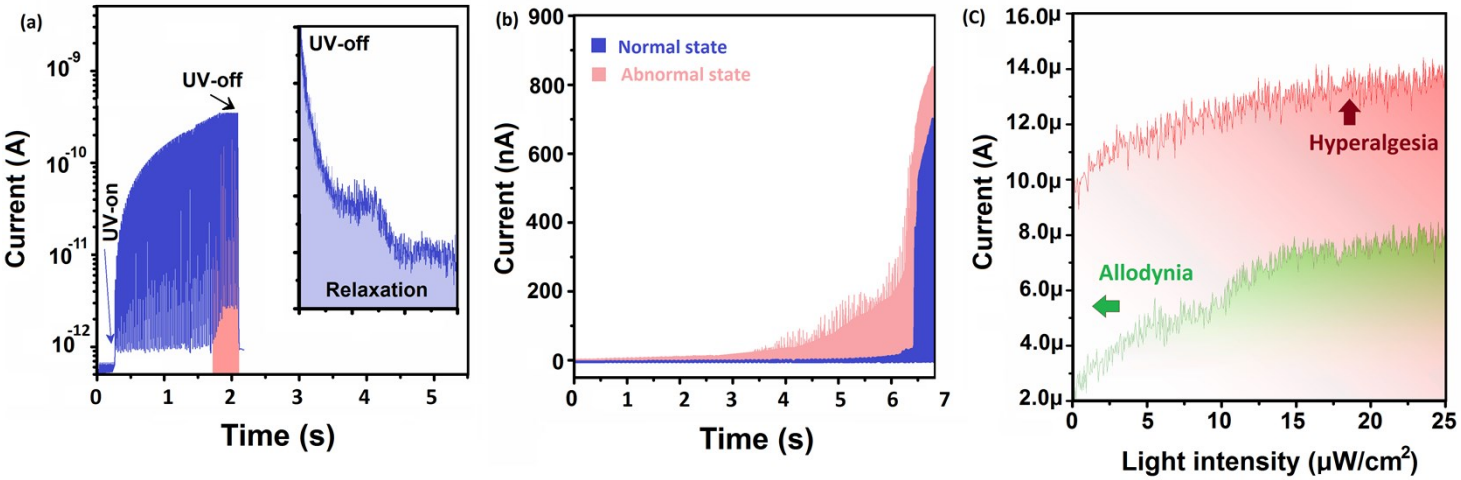

Supplementary Figure S36. The nociceptive performance of another similar Ga_2O_3 (N_2)-TiO_2 device presented for comparison. (a) The relaxation characteristics of device. (b) The behaviour of device in normal and abnormal state. (c) The hyperalgesia and allodynia characteristics of device.

Table S2: The signal to noise ration of Ga_2O_3 (N_2)-TiO_2 normal nociceptor devices for λ= 655 nm light at on-state and saturation condition for different light intensities.

Light power intensity (μW/cm²)	Signal to noise ratio
5	11×10^6
10	25×10^6
15	78×10^6
20	91×10^6

References:

1. V. S. Fomenko, G. V. Samsonov, Handbook of thermodynamic properties, electronic work functions and Richardson constants of elements and compounds, Plenum Press data Division, NewYork • 1966
2. L. A. M. Lyle, L Jiang, K. K. Das, L. M. Porter. Schottky contact to β-Ga2O3. Chapter in: S. Pearton, F. Ren, M. Mastro, Gallium oxide technology, device and applications, 1st ed. *Elsevier Science,* 2019.
3. K. Sasaki, et al., *IEEE Electron Device Lett.* 2013, **34,** 493.
4. M. Amine Kadaoui, W. B. Bouiadjra, A. Saidane, S. Belahsene, A. Ramdane, *Superlattice. Microst.* 2015, **82**, 269.
5. S. M. Sun, W. J. Liu, Y. P. Wang, Y. W. Huan, Q. Ma, B. Zhu, S. D. Wu, W. J. Yu, R. H. Horng, C. T. Xia, Q. Q. Sun, S. J. Ding, D. W. Zhang. *Appl. Phys. Lett.* 2018**, 113**, 031603.
6. E. A. Kraut, R. W. Grant, J. R. Waldrop, S. P. Kowalczyk. *Phys. Rev. B.* 1983, **28**, 1965.